Spin-caloritronic transport in hexagonal graphene nanoflakes

Thị Thu Phùng [1,2] Robert Peters,[3] Andreas Honecker [1] Guy Trambly de Laissardière [1] and Javad Vahedi [1,4,5]

[1]*Laboratoire de Physique Théorique et Modélisation, CNRS UMR 8089, CY Cergy Paris Université, 95302 Cergy-Pontoise Cedex, France*

[2]*Department of Advanced Materials Science and Nanotechnology, University of Science and Technology of Hanoi, 18 Hoang Quoc Viet, 100000 Ha Noi, Vietnam*

[3]*Department of Physics, Kyoto University, Kyoto 606-8502, Japan*

[4]*Jacobs University, School of Engineering and Science, Campus Ring 1, 28759 Bremen, Germany*

[5]*Department of Physics, Sari Branch, Islamic Azad University, Sari 48164-194, Iran*

(Received 6 March 2020; revised 26 May 2020; accepted 8 July 2020; published 29 July 2020)

We investigate the spin-dependent thermoelectric effect of graphene flakes with magnetic edges in the ballistic regime. Employing static, respectively, dynamic mean-field theory we first show that magnetism appears at the zigzag edges for a window of Coulomb interactions that increases significantly with increasing flake size. We then use the Landauer formalism in the framework of the nonequilibrium Green's function method to calculate the spin and charge currents in magnetic hexagonal graphene flakes by varying the temperature of the junction for different flake sizes. While in nonmagnetic gated graphene the temperature gradient drives a charge current, we observe a significant spin current for hexagonal graphene flakes with magnetic zigzag edges. Specifically, we show that in the "*meta*" configuration of a hexagonal flake subject to weak Coulomb interactions, a pure spin current can be driven just by a temperature gradient in a temperature range that is promising for device applications. Bigger flakes are found to yield a bigger window of Coulomb interactions where such spin currents are induced by the magnetic zigzag edges, and larger values of the current.

DOI: 10.1103/PhysRevB.102.035160

I. INTRODUCTION

The thermoelectric effect, i.e., the direct conversion of a temperature difference to an electric voltage and vice versa, attracts great attention in recent years with the development of electronics and spintronics. Many investigations have addressed the fundamental physics and potential applications of thermoelectric phenomena; see, e.g., Refs. [1,2]. With shrinking the size of electronic devices to molecular-scale electronics [3] beyond the foreseen Moore's law limits of small-scale conventional silicon integrated circuits, heat dissipation becomes a severe problem due to a high energy consumption [4]. On the one hand, converting the dissipated heat to electric energy via the thermoelectric effect is an interesting solution to this problem. On the other hand, in the field of spintronics, the coupling of spin and charge transport provides another excellent possibility to reduce the energy dissipation in nanoscale devices [5,6]; the emergent field of *spin caloritronics* promises new functionality exploiting the interplay of spin and heat currents [7,8]. Many works in this field have shown that spin caloritronics would be a viable scheme to realize low power consumption in molecular-scale electronics [9–11].

In recent years, graphene has attracted a tremendous amount of attention, mostly due to its peculiar electronic structure with massless Dirac cones at the Fermi level [12–14]. Graphene is generally believed to be a semimetal with at most weak electronic correlations. Nevertheless, intriguing theoretical investigations made even before single-layer graphene was isolated for the first time [15] predicted that states localized at zigzag edges give rise to magnetic instabilities even when the bulk is semimetallic [16–18]. This edge magnetism arises thanks to electronic states that are localized close to a zigzag edge [19,20] and the fact that only one of the two graphene sublattices participates in a zigzag edge, thus favoring a ferromagnetic alignment of the resulting magnetic moments.

Graphene's distinguished thermal and electronic performance render it one of the most outstanding candidates in spin caloritronics. Many experimental and theoretical works have investigated the thermally induced spin-transport properties of graphene [21–36]. Some of these works [21–27] focused on the electronic properties of graphene. In particular, the sign inversion behavior of graphene's thermoelectric power (TEP) across the charge neutrality point and the gate dependence of the TEP have been measured by Zuev *et al.* [21]. The Seebeck coefficient and the Nernst coefficient have been explored in multiprobe graphene junctions, and both of them show oscillating behavior versus gate voltage [22,23]. The effects of a substrate on the TEP have also been explored by depositing graphene on boron nitride to suppress the disorder, which has led to a large enhancement of the TEP [24]. The charge and spin Seebeck effects in ferromagnetic graphene have been studied by one of the present authors, showing that a pure spin current with a large spin figure of merit is attainable by varying the spin splitting, temperature, and doping of the junction [25]. Further studies concern rectangular rings [26] and bilayer graphene flakes [27].

Another part of the aforementioned investigations [28–36] focused on the effect of the magnetism arising at zigzag edges [16–18,37] on transport properties. In particular, the spin Seebeck effect in graphene nanoribbons has been explored by first-principles calculations [28,30] and mean-field theory [29]. Other geometries that have been considered include

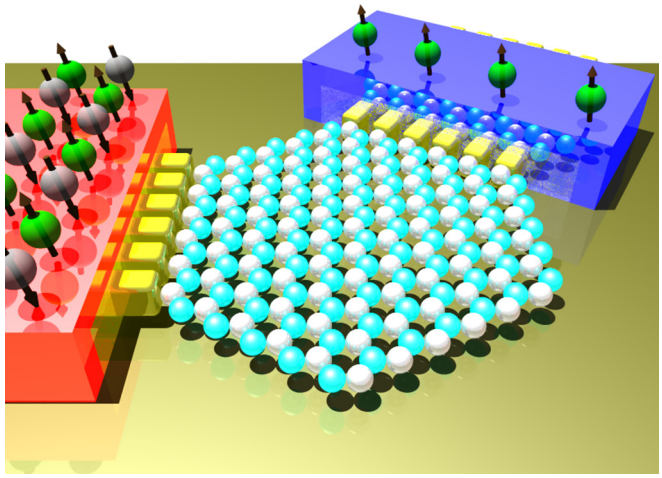

FIG. 1. Cartoon showing a hexagonal zigzag-edge graphene nanoflake (ZGNF) attached to semi-infinite metallic leads to which a temperature difference ΔT is applied. Left and right lead are considered to be hot and cold, respectively. Sublattices A and B are drawn in cyan and white color, respectively. In this cartoon, metallic leads are connected to the sublattice B at different edges in analogy to the *meta* configuration of a benzene molecule.

nanoribbons with sawtooth-modulated edges [31], nanowiggles [32], trapezoidal-shaped nanoribbons [33], nanoporous [38], and also doped ferromagnetic zigzag graphene nanoribbons [39] exhibiting interesting effects on the spin thermopower and an enhancement of the figure of merit. The spin-dependent Seebeck effect has also been studied in other lattices with a honeycomb structure, such as α-silicene nanoribbons [34], zigzag graphyne nanoribbons [35], graphene-based magnetic molecular junctions [36], and magnetic carbon-based organic chains [40].

An important class of systems is given by hexagonal zigzag-edge graphene nanoflakes (ZGNFs) where the magnetic polarization alternates between neighboring edges [41–46]. Recently, Valli *et al.* [47,48] showed that the magnetic edges can yield a nearly complete spin polarization of the current and proposed ZGNFs as efficient spin-filtering devices.

In this paper, we propose a spin-caloritronics device based on hexagonal ZGNFs bridged between two nonmagnetic metallic leads. In this scheme, metallic leads are coupled to the same atomic sublattices of graphene, in the same manner as in the *meta* configuration of a benzene molecular junction [49–51]; see Fig. 1 for a sketch. We demonstrate that, by applying a temperature gradient between the two leads, pure spin currents can be established whose magnitude depends on the reference temperature and the gate voltage. We note that such a spin-energy off-diagonal effect is very different from the aforementioned spin-filtering effect [47,48]. Nevertheless, the main ingredient underlying both of these spin-transport effects are the electronic correlations giving rise to magnetism at the zigzag edges in hexagonal ZGNFs [41–46].

The remainder of this paper is organized as follows. Section II introduces the model and the formalism. In Sec. III we present and discuss numerical results. Finally, Sec. IV provides a summary and conclusions.

II. MODEL AND FORMALISM

Here we study a hexagonal ZGNF attached to conducting metallic leads. The leads are connected to atoms at the edges belonging to the same sublattice, as shown with white color in Fig. 1. Moreover, we consider a temperature gradient ΔT between the two leads.

A. Model

The total Hamiltonian describing the device is given by

$$\mathcal{H} = \mathcal{H}_L + \mathcal{V}_L + \mathcal{H}_C + \mathcal{H}_R + \mathcal{V}_R, \tag{1}$$

where $\mathcal{H}_{L/R} = \sum_{\alpha k\sigma} c^\dagger_{\alpha k\sigma} c_{\alpha k\sigma}$ corresponds to the left (right) metallic lead. $c^\dagger_{i\sigma}$ ($c_{i\sigma}$) creates (annihilates) an electron at site i in the lead $\alpha = L/R$. The term $\mathcal{V}_{L/R} = \sum_{\alpha ik\sigma} (V_{\alpha ik\sigma} c^\dagger_{\alpha k\sigma} a_{i\sigma} +$ H.c.) describes the coupling between the central region and the leads, where $V_{\alpha ik\sigma}$ denotes the hopping amplitude between site i of the central region and state k of lead $\alpha = L/R$. The term $\mathcal{H}_C$ describes the central region for which we use the Hubbard model,

$$\mathcal{H}_C = -t \sum_{i,j,\sigma} a^\dagger_{i\sigma}\, a_{j\sigma} + U \sum_i \left(n_{i\uparrow} - \frac{1}{2}\right)\left(n_{i\downarrow} - \frac{1}{2}\right), \tag{2}$$

where $a^\dagger_{i\sigma}$ ($a_{i\sigma}$) are fermion creation (annihilation) operators, and the number operator is given by $n_{i\sigma} = a^\dagger_{i\sigma} a_{i\sigma}$ with spin σ at site i. The Coulomb-interaction term has been chosen such that the grand-canonical ensemble naturally yields a half-filled charge-neutral system.

The hopping integral for nearest neighbors is well known to be $t \approx 2.7$ eV [12,37]. Since infinite graphene sheets are nonmagnetic, the local Coulomb interaction U has to be sufficiently weak to avoid a bulk magnetic instability, but there is no consensus in the literature regarding its precise value. Magnetic resonance measurements of neutral soliton states in *trans-polyacetylene* have estimated the range $U/t = 1.1$–1.3 [52,53] for sp^2 carbon systems. First-principle studies based on the local density approximation yield $U/t \approx 0.9$, while the generalized gradient approximation (GGA) leads to $U/t \approx 1.3$ [54], and a combination of GGA with a constrained random-phase approximation gives an onsite Coulomb repulsion $U \approx 9.3\,\text{eV} \approx 3.4\,t$ dressed by some longer-range interactions [55]. In view of this uncertainty, we will analyze a range of Coulomb interactions for different hexagonal-ZGNF device sizes.

B. Transport formalism

Electrons need to cross distances of less than 100 atoms when passing through the nanoflakes that we are going to study here. It is therefore reasonable to assume that they will not be scattered inside the device and thus to treat transport as ballistic. Following the Landauer-Büttiker formalism [56], the spin-resolved current thus reads

$$I_\sigma = \frac{e}{h} \int_{-\infty}^{\infty} \mathcal{T}_\sigma(\epsilon)[f_L(\epsilon, T_L) - f_R(\epsilon, T_R)]\, d\epsilon, \tag{3}$$

where $f_\alpha(\epsilon, T_\alpha)$ is the Fermi-Dirac distribution function at the lead $\alpha = L/R$. $\mathcal{T}_\sigma(\epsilon)$ is the spin-resolved transmission for electrons with energy ϵ evaluated by using the nonequilibrium

Green's function approach,

$$\mathcal{T}_\sigma(\epsilon) = \mathrm{Tr}\big[\mathbf{\Gamma}_L(\epsilon) G^r_\sigma(\epsilon) \mathbf{\Gamma}_R(\epsilon) G^a_\sigma(\epsilon)\big], \tag{4}$$

where $\mathbf{\Gamma}_\alpha(\epsilon) = -i[\mathbf{\Sigma}_\alpha - \mathbf{\Sigma}^\dagger_\alpha]$ is the level broadening caused by the coupling between the lead $\alpha = L, R$ and the central region. G^r_σ and G^a_σ are the retarded and advanced Green's functions, respectively. We note that in the case of the ZGNFs with N sites, both the Green's functions and the $\mathbf{\Gamma}_\alpha$ in (4) are $N \times N$ matrices. In general, the functional form of $\mathbf{\Gamma}_\alpha(\epsilon)$ depends on the details of the hybridization between the electrodes and the central region. However, for metals such as gold, the density of states is approximately constant near the Fermi energy such that the wide-band limit is a good approximation [56]. In the wide-band limit, the $\mathbf{\Gamma}_\alpha(\epsilon)$ are replaced by constant matrices $\mathbf{\Gamma}_\alpha(\epsilon) = \mathbf{\Gamma}_\alpha$, where only the diagonal entries corresponding to the left or right edge to which the respective lead is attached are nonzero. In the following, we choose a symmetric coupling such that the nonvanishing matrix elements of $\mathbf{\Gamma}_\alpha$ all take the same value Γ. Furthermore, we will focus on the value $\Gamma = 0.02\,t$ that has been used in a previous investigation of the $N = 54$ ZGNF [47]. The Green's function needed for the transport computations will be calculated both by static mean-field theory (MFT) and a real-space dynamical mean-field theory (rDMFT).

C. Static mean-field theory

Static MFT is a well-established method (see, e.g., Chap. 3.1 of [37]) and has been employed in previous transport computations for graphene nanodevices [29,31,33]. The MFT approximation yields an effective noninteracting problem which allows the calculation of transport coefficients with a standard noninteracting nonequilibrium Green's function method. In this approximation, the Hamiltonian of the central region (2) is written as $\mathcal{H}^{\mathrm{MF}}_C = -t \sum_{i,j,\sigma} a^\dagger_{i\sigma} a_{j\sigma} + U \sum_{i\sigma} n_{i\sigma} \langle n_{i\bar{\sigma}} \rangle$. Thus, the retarded Green's functions of the central region are given by

$$G^r(\epsilon) = \big[(\epsilon + i\eta)\mathbb{1} - \mathcal{H}^{\mathrm{MF}}_C - \mathbf{\Sigma}_L(\epsilon) - \mathbf{\Sigma}_R(\epsilon)\big]^{-1}, \tag{5}$$

where η is an infinitesimal real number, and $\mathbb{1}$ is the identity matrix. The expectation values of the occupation number $\langle n_{i\bar{\sigma}} \rangle$, acting as mean field, need to be calculated self-consistently. This is done by calculating the local density of states $\rho_{i\sigma}(\epsilon) = -\mathrm{Im}\,\mathrm{Tr}[G^r_{i\sigma}(\epsilon)]/\pi$ for an electron at site i with spin σ. The expectation values of the occupation operator then reads $\langle n_{i\bar{\sigma}} \rangle = \int_{-\infty}^{\epsilon_F} \rho_{i\sigma}(\epsilon)\,\mathrm{d}\epsilon$. By combining this equation with Eq. (5), we obtain a set of self-consistency equations that are solved numerically by iteration. This self-consistent solution provides the local spin densities $m^z_i = (n_{i\uparrow} - n_{i\downarrow})/2$ on each site.

We note that MFT has been demonstrated to be remarkably accurate for static [44] and in particular dynamic properties [57] in the semimetallic phase. One of the main shortcomings of static MFT is at the quantitative level when approaching the transition U_c from the semimetallic phase to the antiferromagnetic insulator. For example, the transition point is located at $U^{\mathrm{MFT}}_c/t \approx 2.23$ in MFT [58] while more sophisticated and accurate methods place it in the region $U_c/t \approx 3.8$ [59–62].

D. Dynamical mean-field theory

The quantitative renormalization upon approaching the transition U_c is in turn captured remarkably well by inclusion of local charge fluctuations [63] in the framework of a single-site dynamical mean-field theory [64]. Thus, in order to improve quantitative accuracy with respect to U, here we also employ real-space dynamical mean field theory (rDMFT) to obtain a magnetic solution of the graphene flake.

rDMFT is a nonperturbative approach which maps the lattice Hamiltonian Eq. (2) onto a set of quantum impurity models [64]. This mapping is performed by calculating the local Green's functions of all lattice sites,

$$G^r_i(z) = (z - H_0 - \mathbf{\Sigma}^r(z))^{-1}_{ii}, \tag{6}$$

where H_0 is the single-particle part of Eq. (2) and $\mathbf{\Sigma}^r(z)$ the retarded self-energy matrix. The index i corresponds to a lattice site. The local Green's function for lattice site i can be written as

$$G^r_i(z) = \frac{1}{z - \Delta_i(z) - \Sigma^r_i(z)}, \tag{7}$$

where $\Sigma^r_i(z)$ is the retarded local self-energy of this lattice site. This equation defines a hybridization function $\Delta_i(z)$ for each lattice site, which can be used to set up a single-impurity Anderson model. We use the numerical renormalization group (NRG) to solve these impurity models and obtain the self-energies for all lattice sites [65–67]. The obtained self-energies are used to calculate new local Green's functions according to Eq. (6). Equations (6) and (7), together with the NRG, are iterated until self-consistency is reached. In this way, rDMFT can be used to calculate magnetic solutions of finite clusters [68,69].

Using NRG for finding the self-energies gives us immediate access to real-frequency Green's functions and self-energies with high accuracy around the Fermi energy [70]. After self-consistency is reached, we can use these Green's functions and self-energies to evaluate the transmission coefficient, Eq. (4). We use the Dyson equation $G(\epsilon)^{-1} = G_0(\epsilon)^{-1} - \mathbf{\Sigma}_L(\epsilon) - \mathbf{\Sigma}_R(\epsilon) - \mathbf{\Sigma}(\epsilon)$, where $G_0(\epsilon)^{-1}$ is the bare Green's function of the central region, and $\mathbf{\Sigma}(\epsilon)$ is the self-energy obtained by NRG.

We note that, thanks to a logarithmic energy discretization, NRG yields high frequency resolution close to the Fermi energy, but lower resolution at higher energies; see Ref. [67] for details.

III. RESULTS

In this chapter we present our results for the transport properties of hexagonal ZGNFs. However, before we do so, we briefly revisit their magnetic properties.

A. Edge magnetism of hexagonal ZGNFs

Hexagonal ZGNFs constitute a well-studied example [41–46] of magnetism at zigzag edges. Here we illustrate this with the flake shown in Fig. 2. This flake contains $N = 600$ carbon atoms and is thus bigger than most examples previously studied in the literature [41–44,46]. The localized electronic states at the edges of the ZGNFs lead to a nonuniform spatial profile of the local magnetic moments

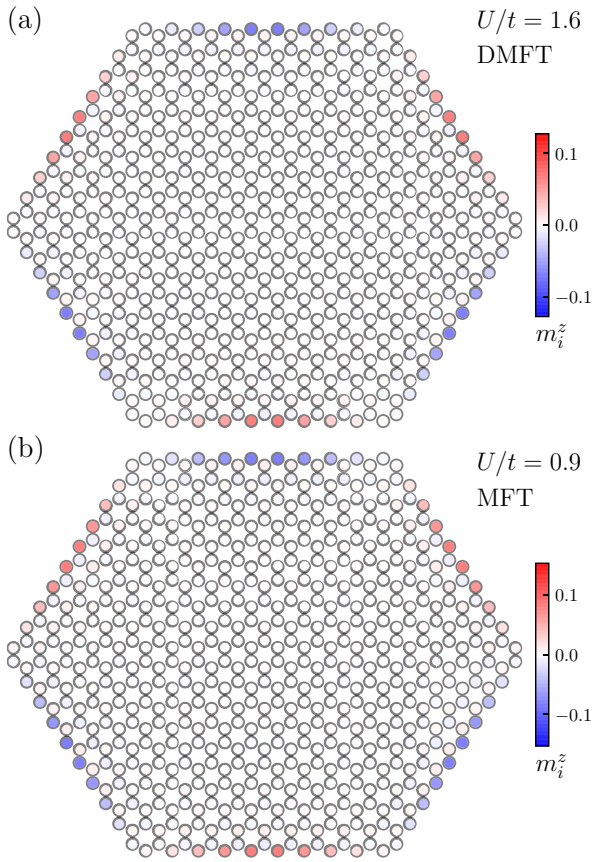

FIG. 2. Spatial magnetization profile for a flake of size $N = 600$ based on (a) DMFT ($U/t = 1.6$) and (b) MFT ($U/t = 0.9$).

$\langle m_i^z \rangle$ which are also mainly localized on the outermost sites. This is illustrated by the color scale in Fig. 2 that shows the magnetic moments for the hexagonal ZGNF with $N = 600$ sites. One observes that spins align ferromagnetically at each edge already for a value of $U/t = 1.6$ ($U/t = 0.9$), well below the bulk (D)MFT critical value $U_c^{\mathrm{DMFT}}/t = 3.5 \ldots 3.7$ [63] ($U_c^{\mathrm{MFT}}/t \approx 2.23$ [58]). This ferromagnetic alignment corresponds to all carbon atoms on each edge belonging to the same sublattice. Adjacent edges are separated by an armchair defect, belong to different sublattices, and thus have opposite magnetization. We note that the magnetic pattern in Fig. 2 is very similar for DMFT and MFT, just the value of the Coulomb interaction is renormalized, as expected from a previous investigation of infinite graphene sheets [63].

Given that the magnetic moment is localized at the edge, its relative contribution to the total staggered magnetization of the flake will vanish in the thermodynamic limit below the bulk critical U_c. Therefore, we characterize this phenomenon by the average staggered magnetization,

$$M_s = \frac{1}{N_{\mathrm{edge}}} \sum_{i \in \mathrm{edge}}^{N_{\mathrm{edge}}} \zeta_i \langle m_i^z \rangle, \tag{8}$$

at the edge where $\zeta_i = 1$ (-1) for i in the A (B) sublattice. Figure 3 shows MFT results for M_s, and one observes that the critical point where the edge of the hexagonal ZGNF becomes magnetic decreases considerably with increasing

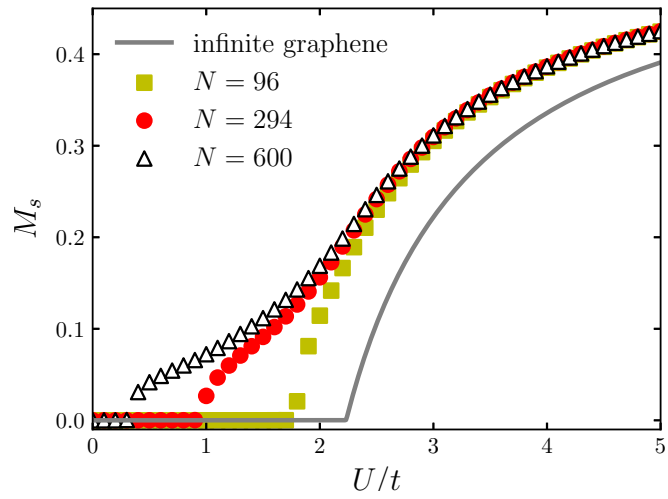

FIG. 3. Average staggered magnetization M_s of edge sites versus U/t based on MFT. Three different sizes are shown by symbols; the gray line shows the staggered magnetization for an infinite graphene sheet.

size. At the biggest size $N = 600$ studied here, the critical point shifts down to the range $U_c^{\mathrm{MFT}}/t|_{N=600} \approx (0.3\text{–}0.4)$, which is far below the critical point of bulk graphene (compare the gray curve in Fig. 3). This critical point is also significantly below the lower bounds for the on-site Coulomb repulsion $U/t \approx 1$ in graphene [52–54], already mentioned in Sec. II A. Figure 2(b) shows that magnetic edges appear for the $N = 600$ ZGNF already for $U/t \leqslant 1.6$ within real-space DMFT. Further calculations (not shown here) show a shift of the critical point within rDMFT to a renormalized range $U_c^{\mathrm{DMFT}}/t|_{N=600} \approx (1.2 - 1.5)$ for the $N = 600$ system. This range is again well below the corresponding estimate for the bulk critical point $3.5 \lesssim U_c^{\mathrm{DMFT}}/t \lesssim 3.7$ [63]. However, this presumably more realistic estimate now becomes comparable to the estimates of the Coulomb interaction. One nevertheless concludes that the magnetic instability at the zigzag edges can be observed in a range of on-site Coulomb interactions that are realistic for graphene, and that the balance could be shifted to even smaller $U_c|_N$ by going to larger sizes $N > 600$.

The magnetic state located at the edge of a ZGNF is closely related to the single-particle level closest to the Fermi energy in the regime $U_c|_N \leqslant U < U_c$. This level is separated from the Fermi energy by a single-particle gap Δ_{sp}. Some values of this gap for the noninteracting ($U = 0$) system are quoted in Table I. One observes that this single-particle gap decreases rapidly with increasing size of the flake N, thus giving rise to the reduction of $U_c|_N$ with growing N observed in Fig. 3

TABLE I. Single-particle gap Δ_{sp} for noninteracting electrons ($U = 0$) on a hexagonal ZGNF as a function of its size N.

N	Δ_{sp}/t
54	0.342 041
96	0.229 448
294	0.072 607
600	0.021 013

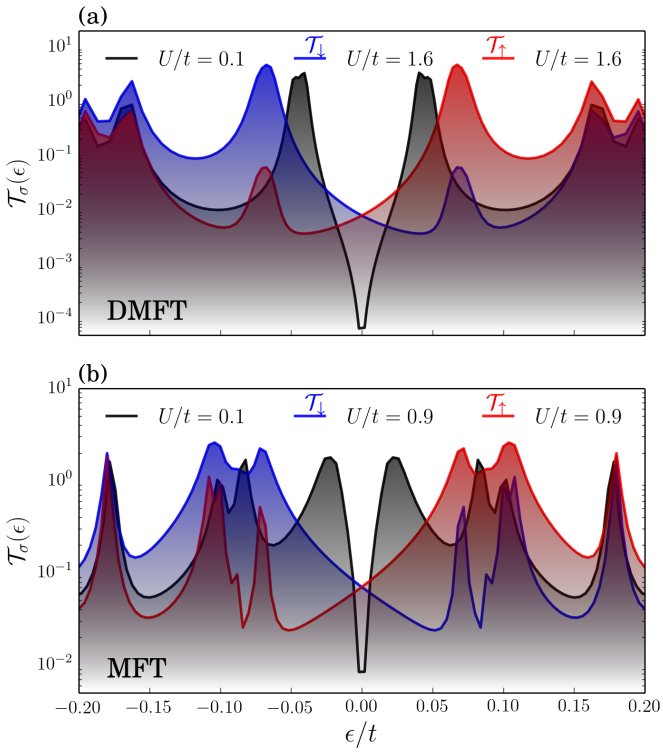

FIG. 4. Spin-resolved transmission coefficients $\mathcal{T}_\sigma$ calculated by (a) DMFT and (b) MFT as a function of ϵ/t for the *meta* configuration of a hexagonal ZGNF with size $N = 600$. The coupling to the leads was taken to be $\Gamma = 0.02\,t$. In both panels, the gray curve is for a Coulomb interaction $U/t = 0.1$ that is below the edge critical value $U_c|_{N=600}$. The values $U/t = 1.6$ and 0.9 in (a) and (b), respectively, lie between $U_c|_{N=600}$ and the bulk critical value U_c. In the latter case, the red and blue curves are the transmission functions $\mathcal{T}_\uparrow$ and $\mathcal{T}_\downarrow$ in the two different spin channels.

and discussed above; see also Chap. 3.3 of Ref. [71]. We note that this reduction of the critical $U_c|_{N=54}$ relative to the bulk value of U_c is almost absent for the $N = 54$ flake studied in Refs. [46–48].

B. Spin-resolved transmission in hexagonal ZGNFs

Next, we use MFT and rDMFT to compute the transmission functions of the flakes. As mentioned in Sec. II, rDMFT is more expensive, but expected to yield a quantitatively more accurate account of the Coulomb integration U in the Hubbard model (2).

Figures 4(a) and 4(b) show the DMFT and MFT results of the spin-resolved transmission $\mathcal{T}_\sigma(\epsilon)$ in the *meta* configuration as a function of the energy of the electrons, respectively. We compare results for two values of the Coulomb interaction; one interaction strength is larger than the critical value $U_c|_N$ for this flake size, the other is smaller. In the former case, the transmission functions shown in Fig. 4 correspond to the magnetic states shown previously in Fig. 2. The main difference between MFT and DMFT is the renormalization by charge fluctuations from $U/t = 0.9$ in MFT to $U/t = 1.6$ in DMFT. The broadening observed in Fig. 4 is due first to the coupling to the leads, $\Gamma = 0.02\,t$. For the MFT computation we chose $\eta = 10^{-6}\,t \ll \Gamma$ such that its effect is negligible. However, in the framework of DMFT there is an additional nonuniform broadening in particular at higher energies $|\epsilon|$, owing to the logarithmic frequency resolution of the NRG impurity solver (see discussion at the end of Sec. II D).

According to Fig. 2, the *meta* configuration corresponds a situation where the leads in Fig. 1 are attached to edges with the same magnetic polarization. Thus, for sufficiently large Coulomb interaction, the hexagonal ZGNF is magnetically ordered and the spin degeneracy is lifted resulting in a distinct spin-dependent transmission $\mathcal{T}_\sigma(\epsilon)$. While the asymmetric transmission spectra for each spin direction $\mathcal{T}_\sigma(\epsilon) \neq \mathcal{T}_\sigma(-\epsilon)$ gives rise to the spin Seebeck effect reported in recent works [72,73], the particle-hole symmetry of the transmission coefficient $\mathcal{T}_\sigma(\epsilon) = \mathcal{T}_{\bar{\sigma}}(-\epsilon)$ under spin inversion leads to a pure spin current, as is discussed later. Figure 4 also shows that in the nonmagnetic state an antiresonance (a deep valley) appears at the Fermi energy in the *meta* configuration. We have checked other possible configurations of the leads (results not shown here), where the leads would be attached to edges of different spin polarization in Fig. 2, that are known as *ortho* and *para* configuration [74], and found no spin-dependent transmission. Thus, in the following, we present results only for the *meta* configuration.

The lowest peaks in Fig. 4 appear at $|\epsilon| \approx 0.07\,t$ for $U/t = 1.6$ and 0.9 in DMFT and static MFT, respectively. This corresponds to a single-particle gap of approximately $0.07\,t$, that is filled in by the coupling to the leads, $\Gamma = 0.02\,t$. Note that the single-particle gap $\Delta_{\rm sp}$ is already enhanced significantly as compared to its noninteracting value even by these moderate values of the Coulomb interaction; see Table I. The temperature scale corresponding to the values of $\Delta_{\rm sp} \approx 0.07\,t$ is on the order of 2200 K and thus significantly higher than the temperatures that we will study below. Indeed, we have checked that a temperature of $T/t = 1/100$ has no visible effect on the MFT results for the magnetic state shown in Fig. 2(b) and should thus also be negligible for the transmission functions shown in Fig. 4. This justifies using these zero-temperature transmission functions to compute finite-temperature transport properties, as we will do in the following.

C. Spin-resolved current in hexagonal ZGNFs

Having calculated the spin-resolved transmission functions, we calculate the current with Eq. (3). Figure 5 shows the spin-up and spin-down currents as a function of the temperature $T = T_L$ for several fixed temperature differences, $\Delta T = T_L - T_R$, between the leads. As can be seen, spin-up ($I_\uparrow$) and spin-down currents ($I_\downarrow$) are of different sign but identical magnitude. The values of U/t are chosen in each case such as to yield magnetic edges without rendering the bulk of the flake magnetic. We recall that MFT has a higher frequency resolution, but we expect DMFT to provide a more accurate description of Coulomb interactions, and that the values of $U/t = 0.9$ and 1.6 in Figs. 5(c) and 5(d) were chosen such as to account for the renormalization by charge fluctuations. After this renormalization, the shape of the curves becomes very similar, as is to be expected given the similarity of the underlying transmission functions already seen in Fig. 4.

We note that the absolute value of the currents in Fig. 5 depends on the choice of Γ, not only explicitly in Eq. (4),

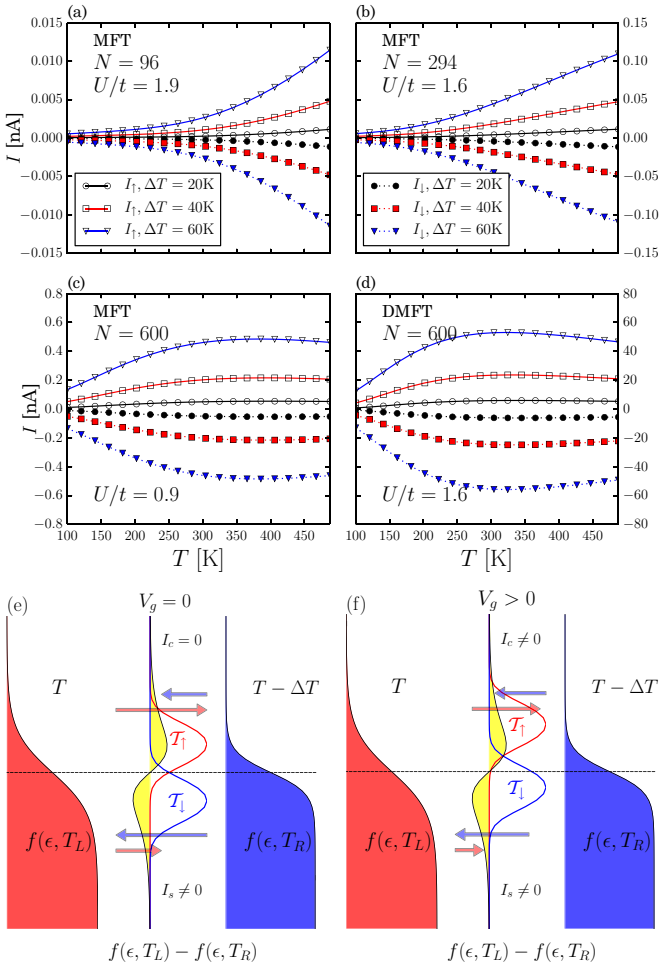

FIG. 5. Spin-resolved current versus temperature T for several temperature differences ΔT and flakes of size (a) $N = 96$, (b) $N = 294$, and (c) and (d) $N = 600$. Note the different vertical scales of the different panels. The coupling to the leads has been chosen as $\Gamma = 0.02\,t$. Panels (a)–(c) are based on MFT; (d) is based on DMFT. The value of U/t is adjusted according to Fig. 3 (compare also the discussion in the main text). (e) and (f) The Fermi-Dirac distributions of the hot and cold leads, respectively, for a gate voltage $V_g = 0$ (e) and $V_g > 0$ (f); the spin-resolved transmission functions are illustrated schematically in the middle between the two Fermi functions. The resulting currents are indicated separately for spin-up (red arrows) and spin-down electrons (blue arrows), as well as for electrons with energies higher (upper set of arrows) and lower (lower set of arrows) than the equilibrium chemical potential (black dotted horizontal line). The yellow filled curve represents the difference of the two Fermi-Dirac distributions.

but also via the Green's functions; see Eq. (5) and recall that $\mathbf{\Sigma}_\alpha \propto i\,\Gamma$. However, we have checked that this only affects the absolute value of I with a power of Γ that appears to be actually lower than 2 while the qualitative temperature dependence of the currents is not very sensitive to the precise value of Γ. In MFT, we chose $\eta = 10^{-6}\,t$ such that this additional broadening becomes irrelevant. However, we recall that the NRG impurity solver for DMFT only yields a logarithmic frequency resolution that cannot be eliminated. The experience with the static MFT indicates that this may lead to an overestimation of the absolute value of the currents in Fig. 5(d) by one to two orders of magnitude, but we still expect the qualitative behavior as a function of temperature to be not very sensitive to the limited energy resolution also in this case.

One observes that the spin currents increase rapidly with temperature for the larger systems, yielding currents that in MFT increase from a few pA to $I \approx 0.5$ nA around room temperature and for a temperature difference $\Delta T = 60$ K, as N increases from 96 to 600. Remarkably, the $N = 600$ flake not only yields the largest current, but also exhibits a maximum of the spin current around room temperature, both within MFT and DMFT; compare Figs. 5(c) and 5(d). The currents set on around a threshold temperature $T_{\mathrm{th},\sigma}$ that is equal for up- and down-spin currents. While $T_{\mathrm{th},\sigma}$ is not very sensitive to the temperature difference ΔT, it exhibits a strong dependence on the size of the hexagonal ZGNF as $T_{\mathrm{th},\sigma}$ decreases significantly with increasing size. For ZGNRs, the size dependence of the threshold temperatures $T_{\mathrm{th},\sigma}$ has been investigated for width 6 and 14, yielding only a slight decrease [28]. This weak dependence of $T_{\mathrm{th},\sigma}$ on the width of ZGNRs can be understood since such ribbons have zero-energy states for $U = 0$ that arise from the infinitely long zigzag edges for any width [16,37,75–77] whereas noninteracting ZGNFs have a finite-size gap in their single-particle spectrum that decreases with increasing N as shown in Table I. However, in contrast to hexagonal ZGNFs, ZGNR-based devices show $T_{\mathrm{th},\uparrow} \neq T_{\mathrm{th},\downarrow}$. Furthermore, these spin currents saturate around room temperature for the $N = 600$ flake. The saturation current for ZGNR-based spin-caloritronics devices is not discussed in the literature, but one can expect it to occur above room temperature, at least for the width-6 and -14 ZGNRs studied in Ref. [28].

The reduction of $T_{\mathrm{th},\sigma}$ can be understood in terms of the overlap of the transmission functions $\mathcal{T}_\sigma(\epsilon)$ with the difference of the Fermi functions $[f_L(\epsilon, T_L) - f_R(\epsilon, T_R)]$ in Eq. (3). Indeed, larger hexagonal ZGNFs have smaller single-particle gaps and thus provide for more transport channels close to the Fermi energy. Thus, one can expect a bigger contribution from the integrand in Eq. (3). This larger overlap leads first to a larger current. Secondly, the reduced energy difference of the transmission peaks and the Fermi energy gives rise to a lower threshold temperature $T_{\mathrm{th},\sigma}$. The relatively low $T_{\mathrm{th},\sigma}$ for the flake size $N = 600$ in Figs. 5(c) and 5(d) can be understood by the energy difference between the highest occupied and lowest unoccupied states shown by the positions of first peaks of the transmission spectrum in Figs. 4(a) and 4(b); compare also the related discussion at the end of Sec. III B, although $T_{\mathrm{th},\sigma}$ is evidently smaller than this bare electronic energy scale.

For a more detailed understanding of the underlying mechanism that generates these currents in the device, we analyze the dependence of the spin current on the Fermi-Dirac distribution functions of the leads and the transmission function in Eq. (3). Figure 5(e) schematically shows the transmission function of the junctions and the Fermi-Dirac distributions of the hot (left) and cold (right) leads. Since $\mathcal{T}_\uparrow(\epsilon)$ is larger above the Fermi energy, charge carriers with high energy flow from the hot lead to the cold lead, giving rise to a positive spin-up current from the hot to the cold lead. Conversely, $\mathcal{T}_\downarrow(\epsilon)$ is much larger below the Fermi energy [Fig. 5(e)] such that the spin-down current flows in the opposite direction.

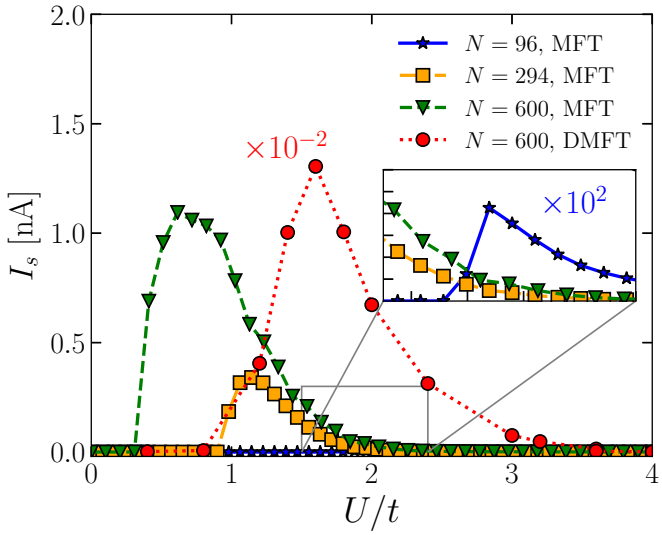

FIG. 6. Dependence of the spin current $I_s = I_\uparrow - I_\downarrow$ on the Coulomb repulsion U/t and flake size at room temperature $T = 300\,\mathrm{K}$ for a fixed temperature difference $\Delta T = 60\,\mathrm{K}$ and coupling to the leads $\Gamma = 0.02\,t$. The inset magnifies a portion of the current where the data for the flake with $N = 96$ sites is multiplied by a factor 100 for better visibility; the DMFT data for $N = 600$ has been divided by 100.

In fact, thanks to the symmetry under the combined particle-hole transformation and spin inversion, the transmission functions satisfy $\mathcal{T}_\sigma(\epsilon) = \mathcal{T}_{\bar\sigma}(-\epsilon)$, where $\bar\sigma$ is the spin projection opposite to σ. This implies that the total charge current, $I_c = I_\uparrow + I_\downarrow = 0$, is exactly zero and the device exhibits a pure spin current, $I_s = I_\uparrow - I_\downarrow \neq 0$.

Returning to the case of ZGNRs, we note that the two opposite edges are individually ferromagnetic in the ground state, but are correlated antiferromagnetically (see Refs. [16,17,37,57,76–78] and references therein). However, a ZGNR-based spin-caloritronics device requires ferromagnetic ZGNRs, at least as long as leads extend over the full width of the ribbon. Consequently, a strong external magnetic field [76], doping, or width engineering [79] is needed to stabilize a ferromagnetic state. From this point of view, the hexagonal-ZGNF junction proposed here has a big advantage over the ZGNRs [28,80,81], and also armchair silicene nanoribbons [82] for spin-caloritronic applications.

D. Effect of the Coulomb interaction

Since the exact value of the Coulomb interaction in hexagonal ZGNFs is unknown, we show the spin current $I_s = I_\uparrow - I_\downarrow$ as a function of on-site Coulomb repulsion U/t in Fig. 6 for three different flake sizes where for $N = 600$ we again compare MFT and DMFT results. We note that $I_\downarrow = -I_\uparrow$ since we are still at charge neutrality (half filling) such that $I_s = 2\,I_\uparrow$. The DMFT results and MFT results in Fig. 6 for the $N = 600$ flake differ by about a factor 100, as we have already seen in the context of Figs. 5(c) and 5(d). We recall that this may be due to an overestimation of the absolute value of the current within DMFT owing to the logarithmic frequency resolution.

A first observation from Fig. 6 is that the spin current vanishes for interaction strengths smaller than the critical point, $U_c|_N$. This is expected because a magnetically ordered edge is needed to establish a spin current. As was already observed in Fig. 3, this critical $U_c|_N$ is size dependent which is also visible in the spin current. For $U > U_c|_N$, the edge becomes magnetic which results in a strong increase of the spin current. Figure 6 shows two curves for the $N = 600$ ZGNF. These two curves have a similar shape; the DMFT curve is just shifted to larger values of U/t with respect to the MFT curve owing to the already mentioned renormalization by charge fluctuations that are ignored in MFT.

Figure 6 also shows again that the maximal attainable spin current grows rapidly with increasing flake size; for the $N = 96$ flake we need to multiply it by 10^2 to render it even visible on the scale of the other curves. For flakes with $N = 600$ sites and the parameters $T = 300\,\mathrm{K}$, $\Delta T = 60\,\mathrm{K}$, the spin current reaches a maximal value $I_s \sim 1\,\mathrm{nA}$ within MFT. However, a further increase of the Coulomb interaction leads to a decrease of the spin current until it vanishes at a specific point which is almost size independent. This interaction strength is close to the bulk critical point of the honeycomb Hubbard model, that is given by $U_c^{\mathrm{MFT}}/t \approx 2.23$ in MFT [58] and $U_c^{\mathrm{DMFT}}/t = 3.5 \ldots 3.7$ [63], respectively. Beyond this bulk critical point, the system becomes an antiferromagnetic Mott insulator and all currents are blocked in the device.

We mention that one can see qualitatively the same behavior for other temperatures $(T, \Delta T)$.

E. Effect of a gate voltage

Finally, we discuss the effect of a gate voltage V_g. We assume that a positive V_g raises the Fermi level of the flake relative to the leads, as sketched in Fig. 5(f), but otherwise has no effect such that we can use the transmission functions $\mathcal{T}_\sigma(\epsilon + V_g)$ that have been obtained at half filling, just shifting their argument by V_g in Eq. (3). We note that when the gate voltage exceeds the single-particle gap, electrons are doped into the system which might change the magnetic state of the flake. We leave a detailed investigation of the interplay of doping and the magnetic state to future studies and focus our discussion on values of the gate voltage inside the gap.

Figure 7 shows the dependence of the spin currents on the gate voltage at room temperature with a fixed temperature difference $\Delta T = 60\,\mathrm{K}$. In each case, we have chosen a value of U such that $U_c^{\mathrm{MFT}}|_N < U < U_c^{\mathrm{MFT}}$. Here we also included an example for $N = 54$ in Fig. 7(a) where the aforementioned condition forces us to choose $U/t = 2.1$, very close to the bulk transition $U_c^{\mathrm{MFT}}/t \approx 2.23$ [58]. Regions where the gate voltage exceeds the single-particle gap are shaded in gray in Fig. 7 and will be excluded from further discussion.

Although the symmetry of the spin-up and spin-down transmission coefficients is preserved, the shift of the chemical potential (i.e., the Fermi level) on the flake results in a situation where the spin-down current is larger than the spin-up current for $V_g > 0$ and vice versa for $V_g < 0$. Indeed, the spin-resolved currents are antisymmetric under spin inversion $I_\sigma(V_g) = -I_{\bar\sigma}(-V_g)$ which leads to a spin current I_s that is even under sign inversion of V_g and a charge current I_c that is odd. Therefore, a pure spin current exists only for

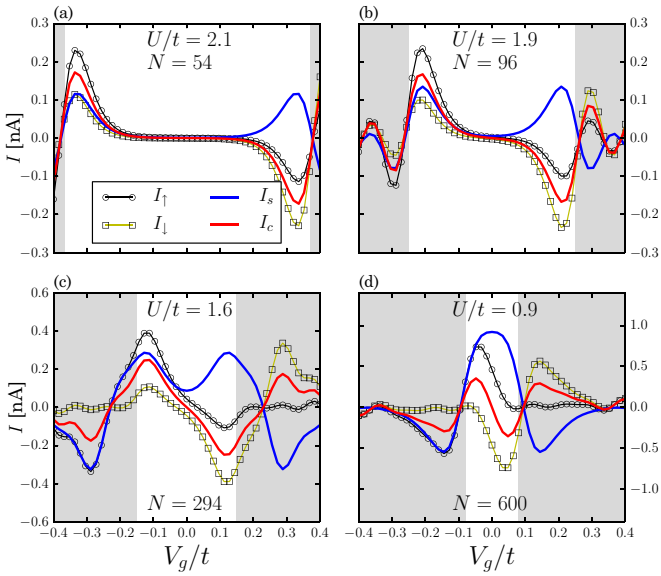

FIG. 7. Spin-resolved current versus gate voltage V_g/t for flakes with sizes (a) $N = 54$, (b) $N = 96$, (c) $N = 294$, and (d) $N = 600$ based on MFT. The temperature is $T = 300\,\mathrm{K}$, the temperature difference is $\Delta T = 60\,\mathrm{K}$, and the coupling to the leads $\Gamma = 0.02\,t$. In each case, we have chosen a value of U such that the edge is magnetic but the bulk of the flake remains nonmagnetic. Note the different vertical scales of the panels.

$V_g = 0$, while generically charge and spin currents both flow for nonzero gate voltages. Moreover, Fig. 7 exhibits a strong size dependence of the response to the gate voltage. In fact, the maxima for the curves for $I_s(V_g)$ are close to the highest (lowest) occupied (unoccupied) level that sits at the border of the shaded region, but still inside the gap. Since the single-particle gap decreases rapidly with increasing flake size N, for flakes with $N = 54$ and $N = 96$ sites, a small gate voltage results in small charge and spin currents, and a gate voltage of $|V_g/t| > 0.2$ is required to induce appreciable charge and spin currents. By contrast, for the larger hexagonal-ZGNF sizes, namely $N = 294$ and $N = 600$, a small gate voltage is sufficient to induce significant currents. In addition, for these larger flakes, the temperature $T = 300\,\mathrm{K}$ leads to an appreciable current in the gaps owing to thermal fluctuations. As we have already seen in Figs. 5(a)–5(d), the maximum current increases with increasing N (note the different scales of the vertical axes in Fig. 7).

IV. CONCLUSION

We have investigated the spin-caloritronic properties of hexagonal ZGNFs. First, we have treated the magnetic properties both by simple static MFT and the more accurate DMFT, providing us with the Green's functions and thus the transmission coefficients of the ZGNFs. The spin-dependent transport was then evaluated by the Landauer formalism in the framework of the nonequilibrium Green's function method. One of our main findings is that a pure spin current can be driven by a temperature gradient in the charge-neutral system if the Coulomb interaction is sufficiently large to render the zigzag edges magnetic, but still sufficiently small such that the bulk remains nonmagnetic, and leads are attached to two edges with the same magnetization in a configuration that resembles the *meta* binding motif in a benzene molecule. We found that the window of Coulomb interactions U where only the edges are magnetic and thus a spin current flows increases significantly as the size of the flakes increases from $N = 96$ to $N = 600$, thus improving chances that the value of the Coulomb interaction in graphene is indeed in the relevant regime. At the same time, the absolute value of the spin current also increases significantly with increasing size of the flake and develops a maximum around room temperature for $N = 600$. These observations promise room-temperature applications of ZGNFs with $N \approx 600$ carbon atoms.

The value of the spin current can be enhanced by an applied gate voltage V_g with a significant effect in particular for the smaller flakes. We note that when the gate voltage exceeds the single-particle gap, electrons are doped into the system such that the magnetic state of the edges might change. Furthermore, doping reduces the gap values such that the effect of thermal fluctuations on the magnetic state may no longer be negligible. We suggest investigation of such effects as an interesting topic for further studies.

It should be mentioned that while dynamic properties are accurately captured by MFT, the static magnetism of the edge is actually an artifact of the mean-field approximation to the Hubbard model [57]. Further ingredients, such as a combination of spin-orbit coupling, external fields, or flakes with different edge lengths, will therefore be needed to stabilize magnetic edges in actual device applications. Furthermore, we have assumed transport to be ballistic and ignored all spin-relaxation and spin-flip processes. This is justified for a device which is smaller than the spin relaxation length. We also assume that all dissipation processes occur in the leads which remains reasonable for even the biggest flakes that we consider in this work. Thus, in order to use devices in a spin-caloritronics application, a length $L < l_{sp} \sim 1\mu\mathrm{m}$ is needed, which is accessible in current experiments [83]. Nevertheless, the thermoelectric effects in graphene-based devices have already been observed with considerable precision [21,22]. On the other hand, a recent experiment used the local magnetoresistance technique to detect the thermoelectric spin voltage in graphene [72], which shows that in principle it is feasible to measure spin-dependent thermoelectric properties.

ACKNOWLEDGMENTS

This work was supported by the Paris//Seine excellence initiative, the 911 project of the Ministry of Education and Training of Vietnam, and the ANR project J2D (Project No. ANR-15-CE24-0017). R.P. is supported by JSPS KAKENHI Grants No. 18K03511 and No. 18H04316. The DMFT simulations were performed on the "Hokusai" supercomputer in RIKEN and the supercomputer of the Institute for Solid State Physics (ISSP) in Japan. R.P. thanks the Université de Cergy-Pontoise and its Institute for Advanced Studies for hospitality during a research visit.

[1] A. Kirihara, K. Uchida, Y. Kajiwara, M. Ishida, Y. Nakamura, T. Manako, E. Saitoh, and S. Yorozu, Spin-current-driven thermoelectric coating, Nat. Mater. **11**, 686 (2012).

[2] Y. Kim, W. Jeong, K. Kim, W. Lee, and P. Reddy, Electrostatic control of thermoelectricity in molecular junctions, Nat. Nanotechnol. **9**, 881 (2014).

[3] A. Aviram and M. A. Ratner, Molecular rectifiers, Chem. Phys. Lett. **29**, 277 (1974).

[4] E. Pop, S. Sinha, and K. E. Goodson, Heat generation and transport in nanometer-scale transistors, Proc. IEEE **94**, 1587 (2006).

[5] S. A. Wolf, D. D. Awschalom, R. A. Buhrman, J. M. Daughton, S. von Molnár, M. L. Roukes, A. Y. Chtchelkanova, and D. M. Treger, Spintronics: A spin-based electronics vision for the future, Science **294**, 1488 (2001).

[6] A. Fert, Nobel lecture: Origin, development, and future of spintronics, Rev. Mod. Phys. **80**, 1517 (2008).

[7] K. Uchida, S. Takahashi, K. Harii, J. Ieda, W. Koshibae, K. Ando, S. Maekawa, and E. Saitoh, Observation of the spin Seebeck effect, Nature (London) **455**, 778 (2008).

[8] H. Adachi, K. Uchida, E. Saitoh, and S. Maekawa, Theory of the spin Seebeck effect, Rep. Prog. Phys. **76**, 036501 (2013).

[9] K. Uchida, J. Xiao, H. Adachi, J. Ohe, S. Takahashi, J. Ieda, T. Ota, Y. Kajiwara, H. Umezawa, H. Kawai, G. E. W. Bauer, S. Maekawa, and E. Saitoh, Spin Seebeck insulator, Nat. Mater. **9**, 894 (2010).

[10] C. M. Jaworski, J. Yang, S. Mack, D. D. Awschalom, J. P. Heremans, and R. C. Myers, Observation of the spin-Seebeck effect in a ferromagnetic semiconductor, Nat. Mater. **9**, 898 (2010).

[11] G. E. W. Bauer, E. Saitoh, and B. J. van Wees, Spin caloritronics, Nat. Mater. **11**, 391 (2012).

[12] A. H. Castro Neto, F. Guinea, N. M. R. Peres, K. S. Novoselov, and A. K. Geim, The electronic properties of graphene, Rev. Mod. Phys. **81**, 109 (2009).

[13] S. Das Sarma, S. Adam, E. H. Hwang, and E. Rossi, Electronic transport in two-dimensional graphene, Rev. Mod. Phys. **83**, 407 (2011).

[14] K. S. Novoselov, V. I. Fal'ko, L. Colombo, P. R. Gellert, M. G. Schwab, and K. Kim, A roadmap for graphene, Nature (London) **490**, 192 (2012).

[15] K. S. Novoselov, A. K. Geim, S. V. Morozov, D. Jiang, Y. Zhang, S. V. Dubonos, I. V. Grigorieva, and A. A. Firsov, Electric field effect in atomically thin carbon films, Science **306**, 666 (2004).

[16] M. Fujita, K. Wakabayashi, K. Nakada, and K. Kusakabe, Peculiar localized state at zigzag graphite edge, J. Phys. Soc. Jpn. **65**, 1920 (1996).

[17] K. Wakabayashi, M. Sigrist, and M. Fujita, Spin wave mode of edge-localized magnetic states in nanographite zigzag ribbons, J. Phys. Soc. Jpn. **67**, 2089 (1998).

[18] K. Wakabayashi, M. Fujita, H. Ajiki, and M. Sigrist, Electronic and magnetic properties of nanographite ribbons, Phys. Rev. B **59**, 8271 (1999).

[19] K. Nakada, M. Fujita, G. Dresselhaus, and M. S. Dresselhaus, Edge state in graphene ribbons: Nanometer size effect and edge shape dependence, Phys. Rev. B **54**, 17954 (1996).

[20] L. Brey and H. A. Fertig, Electronic states of graphene nanoribbons studied with the Dirac equation, Phys. Rev. B **73**, 235411 (2006).

[21] Y. M. Zuev, W. Chang, and P. Kim, Thermoelectric and Magnetothermoelectric Transport Measurements of Graphene, Phys. Rev. Lett. **102**, 096807 (2009).

[22] P. Wei, W. Bao, Y. Pu, C. N. Lau, and J. Shi, Anomalous Thermoelectric Transport of Dirac Particles in Graphene, Phys. Rev. Lett. **102**, 166808 (2009).

[23] J. G. Checkelsky and N. P. Ong, Thermopower and Nernst effect in graphene in a magnetic field, Phys. Rev. B **80**, 081413(R) (2009).

[24] F. Ghahari, H.-Y. Xie, T. Taniguchi, K. Watanabe, M. S. Foster, and P. Kim, Enhanced Thermoelectric Power in Graphene: Violation of the Mott Relation by Inelastic Scattering, Phys. Rev. Lett. **116**, 136802 (2016).

[25] J. Vahedi and F. Barimani, Spin and charge thermopower effects in the ferromagnetic graphene junction, J. Appl. Phys. **120**, 084303 (2016).

[26] M. Saiz-Bretín, A. V. Malyshev, P. A. Orellana, and F. Domínguez-Adame, Enhancing thermoelectric properties of graphene quantum rings, Phys. Rev. B **91**, 085431 (2015).

[27] L. Chico, P. A. Orellana, L. Rosales, and M. Pacheco, Spin and Charge Caloritronics in Bilayer Graphene Flakes with Magnetic Contacts, Phys. Rev. Applied **8**, 054029 (2017).

[28] M. Zeng, Y. Feng, and G. Liang, Graphene-based spin caloritronics, Nano Lett. **11**, 1369 (2011).

[29] Z. Zhao, X. Zhai, and G. Jin, Bipolar-unipolar transition in thermospin transport through a graphene-based transistor, Appl. Phys. Lett. **101**, 083117 (2012).

[30] Y. Ni, K. Yao, H. Fu, G. Gao, S. Zhu, and S. Wang, Spin Seebeck effect and thermal colossal magnetoresistance in graphene nanoribbon heterojunction, Sci. Rep. **3**, 1380 (2013).

[31] X. Chen, Y. Liu, B.-L. Gu, W. Duan, and F. Liu, Giant room-temperature spin caloritronics in spin-semiconducting graphene nanoribbons, Phys. Rev. B **90**, 121403(R) (2014).

[32] L. Liang, E. Cruz-Silva, E. C. Girão, and V. Meunier, Enhanced thermoelectric figure of merit in assembled graphene nanoribbons, Phys. Rev. B **86**, 115438 (2012).

[33] M. Shirdel-Havar and R. Farghadan, Spin caloritronics in spin semiconducting armchair graphene nanoribbons, Phys. Rev. B **97**, 235421 (2018).

[34] K. Zberecki, M. Wierzbicki, J. Barnaś, and R. Swirkowicz, Thermoelectric effects in silicene nanoribbons, Phys. Rev. B **88**, 115404 (2013).

[35] M.-X. Zhai, X.-F. Wang, P. Vasilopoulos, Y.-S. Liu, Y.-J. Dong, L. Zhou, Y.-J. Jiang, and W.-L. You, Giant magnetoresistance and spin Seebeck coefficient in zigzag α-graphyne nanoribbons, Nanoscale **6**, 11121 (2014).

[36] J. Li, B. Wang, F. Xu, Y. Wei, and J. Wang, Spin-dependent Seebeck effects in graphene-based molecular junctions, Phys. Rev. B **93**, 195426 (2016).

[37] O. V. Yazyev, Emergence of magnetism in graphene materials and nanostructures, Rep. Prog. Phys. **73**, 056501 (2010).

[38] Y. Dong, Y. Wu, X. Wang, X. Yang, and Y. Liu, Nanoporous graphene nanoribbons: Robust spin-semiconducting property and perfect spin Seebeck effects, J. Phys. Chem. C **123**, 29126 (2019).

[39] L. Song, S. Jin, Y. Liu, L. Yuan, Z. Yang, P. Jiang, and X. Zheng, Thermal gradient driven spin current in BN co-doped ferromagnetic zigzag graphene nanoribbons, Physica E **115**, 113684 (2020).

[40] F. X. Tan, L. Y. Yang, X. F. Yang, and Y. S. Liu, Thermoelectric transport properties of magnetic carbon-based organic chains, Chem. Phys. **528**, 110524 (2020).

[41] J. Fernández-Rossier and J. J. Palacios, Magnetism in Graphene Nanoislands, Phys. Rev. Lett. **99**, 177204 (2007).

[42] S. Bhowmick and V. B. Shenoy, Edge state magnetism of single layer graphene nanostructures, J. Chem. Phys. **128**, 244717 (2008).

[43] J. Viana-Gomes, V. M. Pereira, and N. M. R. Peres, Magnetism in strained graphene dots, Phys. Rev. B **80**, 245436 (2009).

[44] H. Feldner, Z. Y. Meng, A. Honecker, D. Cabra, S. Wessel, and F. F. Assaad, Magnetism of finite graphene samples: Mean-field theory compared with exact diagonalization and quantum Monte Carlo simulations, Phys. Rev. B **81**, 115416 (2010); **101**, 049909(E) (2020).

[45] B. Roy, F. F. Assaad, and I. F. Herbut, Zero Modes and Global Antiferromagnetism in Strained Graphene, Phys. Rev. X **4**, 021042 (2014).

[46] A. Valli, A. Amaricci, A. Toschi, T. Saha-Dasgupta, K. Held, and M. Capone, Effective magnetic correlations in hole-doped graphene nanoflakes, Phys. Rev. B **94**, 245146 (2016).

[47] A. Valli, A. Amaricci, V. Brosco, and M. Capone, Quantum interference assisted spin filtering in graphene nanoflakes, Nano Lett. **18**, 2158 (2018).

[48] A. Valli, A. Amaricci, V. Brosco, and M. Capone, Interplay between destructive quantum interference and symmetry-breaking phenomena in graphene quantum junctions, Phys. Rev. B **100**, 075118 (2019).

[49] J. S. Meisner, S. Ahn, S. V. Aradhya, M. Krikorian, R. Parameswaran, M. Steigerwald, L. Venkataraman, and C. Nuckolls, Importance of direct metal-π coupling in electronic transport through conjugated single-molecule junctions, J. Am. Chem. Soc. **134**, 20440 (2012).

[50] D. Z. Manrique, C. Huang, M. Baghernejad, X. Zhao, O. A. Al-Owaedi, H. Sadeghi, V. Kaliginedi, W. Hong, M. Gulcur, T. Wandlowski, M. R. Bryce, and C. J. Lambert, A quantum circuit rule for interference effects in single-molecule electrical junctions, Nat. Commun. **6**, 6389 (2015).

[51] J. Liu, X. Huang, F. Wang, and W. Hong, Quantum interference effects in charge transport through single-molecule junctions: Detection, manipulation, and application, Acc. Chem. Res. **52**, 151 (2019).

[52] W. P. Su, J. R. Schrieffer, and A. J. Heeger, Solitons in Polyacetylene, Phys. Rev. Lett. **42**, 1698 (1979).

[53] S.-I. Kuroda and H. Shirakawa, Electron-nuclear double-resonance evidence for the soliton wave function in polyacetylene, Phys. Rev. B **35**, 9380(R) (1987).

[54] T. Bally, D. A. Hrovat, and W. T. Borden, Attempts to model neutral solitons in polyacetylene by *ab initio* and density functional methods. The nature of the spin distribution in polyenyl radicals, Phys. Chem. Chem. Phys. **2**, 3363 (2000).

[55] T. O. Wehling, E. Şaşioğlu, C. Friedrich, A. I. Lichtenstein, M. I. Katsnelson, and S. Blügel, Strength of Effective Coulomb Interactions in Graphene and Graphite, Phys. Rev. Lett. **106**, 236805 (2011).

[56] S. Datta, *Quantum Transport: Atom to Transistor* (Cambridge University Press, Cambridge, 2005).

[57] H. Feldner, Z. Y. Meng, T. C. Lang, F. F. Assaad, S. Wessel, and A. Honecker, Dynamical Signatures of Edge-State Magnetism on Graphene Nanoribbons, Phys. Rev. Lett. **106**, 226401 (2011).

[58] S. Sorella and E. Tosatti, Semi-metal-insulator transition of the Hubbard model in the honeycomb lattice, Europhys. Lett. **19**, 699 (1992).

[59] S. Sorella, Y. Otsuka, and S. Yunoki, Absence of a spin liquid phase in the Hubbard model on the honeycomb lattice, Sci. Rep. **2**, 992 (2012).

[60] S. R. Hassan and D. Sénéchal, Absence of Spin Liquid in Nonfrustrated Correlated Systems, Phys. Rev. Lett. **110**, 096402 (2013).

[61] F. F. Assaad and I. F. Herbut, Pinning the Order: The Nature of Quantum Criticality in the Hubbard Model on Honeycomb Lattice, Phys. Rev. X **3**, 031010 (2013).

[62] D. Hirschmeier, H. Hafermann, and A. I. Lichtenstein, Multiband dual fermion approach to quantum criticality in the Hubbard honeycomb lattice, Phys. Rev. B **97**, 115150 (2018).

[63] M. Raczkowski, R. Peters, T. T. Phùng, N. Takemori, F. F. Assaad, A. Honecker, and J. Vahedi, Hubbard model on the honeycomb lattice: From static and dynamical mean-field theories to lattice quantum Monte Carlo simulations, Phys. Rev. B **101**, 125103 (2020).

[64] A. Georges, G. Kotliar, W. Krauth, and M. J. Rozenberg, Dynamical mean-field theory of strongly correlated fermion systems and the limit of infinite dimensions, Rev. Mod. Phys. **68**, 13 (1996).

[65] K. G. Wilson, The renormalization group: Critical phenomena and the Kondo problem, Rev. Mod. Phys. **47**, 773 (1975).

[66] H. R. Krishna-murthy, J. W. Wilkins, and K. G. Wilson, Renormalization-group approach to the Anderson model of dilute magnetic alloys. I. Static properties for the symmetric case, Phys. Rev. B **21**, 1003 (1980).

[67] R. Bulla, T. A. Costi, and T. Pruschke, Numerical renormalization group method for quantum impurity systems, Rev. Mod. Phys. **80**, 395 (2008).

[68] R. Peters and N. Kawakami, Spin density waves in the Hubbard model: A DMFT approach, Phys. Rev. B **89**, 155134 (2014).

[69] R. Peters and N. Kawakami, Large and small Fermi-surface spin density waves in the Kondo lattice model, Phys. Rev. B **92**, 075103 (2015).

[70] R. Peters, T. Pruschke, and F. B. Anders, Numerical renormalization group approach to Green's functions for quantum impurity models, Phys. Rev. B **74**, 245114 (2006).

[71] T. T. Phùng, Numerical Studies of Magnetism and Transport Properties in Graphene Nano-Devices, Ph.D thesis, Université de Cergy-Pontoise, Cergy, 2019.

[72] J. F. Sierra, I. Neumann, J. Cuppens, B. Raes, M. V. Costache, and S. O. Valenzuela, Thermoelectric spin voltage in graphene, Nat. Nanotechnol. **13**, 107 (2018).

[73] X.-Q. Tang, X.-M. Ye, X.-Y. Tan, and D.-H. Ren, Metal-free magnetism, spin-dependent Seebeck effect, and spin-Seebeck diode effect in armchair graphene nanoribbons, Sci. Rep. **8**, 927 (2018).

[74] A. Borges, J. Xia, S. H. Liu, L. Venkataraman, and G. C. Solomon, The role of through-space interactions in modulating constructive and destructive interference effects in benzene, Nano Lett. **17**, 4436 (2017).

[75] T. Hikihara, X. Hu, H.-H. Lin, and C.-Y. Mou, Ground-state properties of nanographite systems with zigzag edges, Phys. Rev. B **68**, 035432 (2003).

[76] Y.-W. Son, M. L. Cohen, and S. G. Louie, Half-metallic graphene nanoribbons, Nature (London) **444**, 347 (2006).

[77] J. Fernández-Rossier, Prediction of hidden multiferroic order in graphene zigzag ribbons, Phys. Rev. B **77**, 075430 (2008).

[78] G. Z. Magda, X. Jin, I. Hagymási, P. Vancsó, Z. Osváth, P. Nemes-Incze, C. Hwang, L. P. Biró, and L. Tapasztó, Room-temperature magnetic order on zigzag edges of narrow graphene nanoribbons, Nature (London) **514**, 608 (2014).

[79] W.-C. Chen, Y. Zhou, S.-L. Yu, W.-G. Yin, and C.-D. Gong, Width-tuned magnetic order oscillation on zigzag edges of honeycomb nanoribbons, Nano Lett. **17**, 4400 (2017).

[80] X. Zhai, J. Gu, R. Wen, R.-W. Liu, M. Zhu, X. Zhou, L.-Y. Gong, and X. Li, Giant Seebeck magnetoresistance triggered by electric field and assisted by a valley through a ferromagnetic/antiferromagnetic junction in heavy group-IV monolayers, Phys. Rev. B **99**, 085421 (2019).

[81] Y.-Z. Lv and P. Zhao, Spin caloritronic transport of tree-saw graphene nanoribbons, Chin. Phys. Lett. **36**, 017301 (2019).

[82] X.-Y. Tan, D.-D. Wu, Q.-B. Liu, H.-H. Fu, and R. Wu, Spin caloritronics in armchair silicene nanoribbons with sp^3 and sp^2-type alternating hybridizations, J. Phys.: Condens. Matter **30**, 355303 (2018).

[83] M. H. D. Guimarães, J. J. van den Berg, I. J. Vera-Marun, P. J. Zomer, and B. J. van Wees, Spin transport in graphene nanostructures, Phys. Rev. B **90**, 235428 (2014).